Image processing for the experimental investigation of dense dispersed flows: application to bubbly flows

Lucia Rueda Villegas, Damien Colombet, Pascal Guiraud, Dominique
Legendre, Sébastien Cazin, Arnaud Cockx

HAL Id: hal-02139287
https://hal.archives-ouvertes.fr/hal-02139287

Submitted on 24 May 2019

Image processing for the experimental investigation of dense dispersed flows: Application to bubbly flows

L. Rueda Villegas [a,b,c], D. Colombet [a,b,c,*], P. Guiraud [b,c], D. Legendre [a,c], S. Cazin [a,c], A. Cockx [b,c]

[a] *Institut de Mécanique des Fluides de Toulouse, IMFT, Université de Toulouse, CNRS - Toulouse, France*
[b] *LISBP, Université de Toulouse, INSA, INRA, CNRS, Toulouse, France*
[c] *FERMAT, Université de Toulouse, CNRS, INP, INSA, UPS, Toulouse, France*

A B S T R A C T

In this work an image processing technique is proposed to improve the measurement of ellipsoidal objects, such as bubbles in dispersed flows. This novel algorithm devoted to the measurement of bubble size, shape and trajectory is applied to binarised images from a gray-level gradient filter. To improve data statistics, an ellipse fitting method is employed to take into account truncated bubbles at the image edges. Then, an original approach is proposed to enable the segmentation of overlapping bubbles. The complete algorithm is evaluated on synthetic images and on real images for an air-bubble swarm within water. This new and robust methodology enables to increase substantially (more than 40%) the number of bubbles detected and thus to improve data convergence.

1. Introduction

In experimental science, with the increase of data storage and performance of high-speed cameras, self-regulating image processing techniques are crucial for the analysis of all data without human validation. In this paper, we propose an image processing method to automatically identify ellipse-like objects in gray-level images. This method has been developed for the study of rising bubbles in bubbly flows such as observed in bubble columns, specially when the bubble volume fraction defeats classical methods.

Among the large number of papers dealing with the experimental investigation of bubbly flows, some deal with indirect measurements techniques. For instance, Yianatos et al. (1987) adapt Masliyah equations for solid spheres to determine the average diameter of small bubbles (over the range 0.5–2 mm) from the superficial liquid and gas flow rates, and the gas hold-up. Kumar et al. (1976) correlate the average bubble size with experimental data of gas hold-up and interfacial area calculated by the chemical method proposed by Calderbank (1958). However, these methods are not able to determine the bubble size distribution that is crucial for mass transfer prediction.

Direct measurements are performed to that end. They can be either invasive like capillary suction probes, conductivity probes and wire-mesh sensors, or non invasive like Phase Doppler Anemometry, Interferometric Particle Imaging or Shadowgraphy. The present investigation focuses on the analysis of Shadowgraphy images of air bubbles rising in a water column.

Many image processing techniques were developed in order to analyze a bubbly flow. For instance, the bubble-identification method by Akita and Yoshida (1974) leads to an accurate correlation of the average bubble diameter within 15% for different liquids (water, water and glycol, water and glycerol, etc.), various fluid temperatures and liquid parameters (density, viscosity, surface tension, etc.). Burckhart and Deckwer (1975) determine the size distribution of bubbles using two bubble columns with different injectors and liquid solutions. However, these data were obtained manually by measuring bubbles on 3–10 images and obviously data convergence were not satisfactory.

The detection of spherical full objects is usually performed using algorithms based on the Hough transformation in polar coordinates (Duda and Hart, 1972; Davies, 1987). This approach based on a parametric description of the contour enables the calculation of circle center and radius. Although the Hough transformation is very interesting for the detection of spherical objects, it is known to be expensive in time and memory and to be unsuitable for the detection of partially occluded circular shape objects. To overcome this difficulty, Pla (1996) proposed a method based on the calculation of the curvature of objects contours to detect connecting points that correspond to the intersection of two bubble contours: segments having a constant curvature are identified to
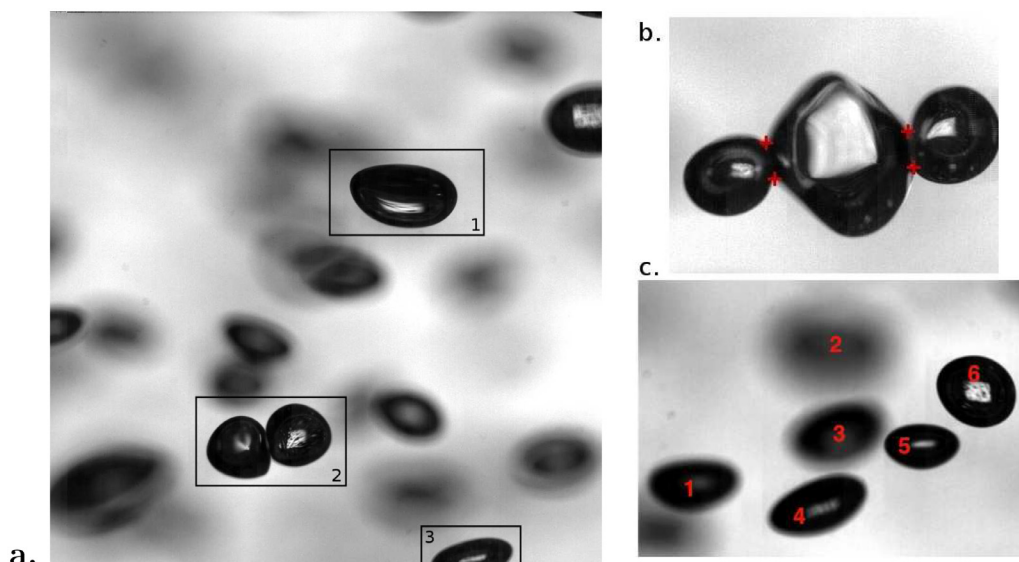
Fig. 1. Gray-level images of a bubbly flow. (a) Single bubbles (box # 1), Overlapping bubbles (box # 2) and Truncated bubbles (box # 3). (b) Inflexion points in overlapping bubbles. (c) In-of-focus (5, 6) and out-of-focus (1, 2, 3, 4) bubbles.

be object contours, then, the overlapping contours are separated thanks to the analysis of the derivative of the curvature. The application of this method on real complex images enables the detection of full and partially occluded spherical objects. However, it can result sometimes in the detection of additional spherical objects that are not present in the original image. An improved method was later proposed by Shen et al. (2000). In their work, to deal with the identification and the treatment of overlapping objects, authors proposed to perform the segmentation of contours by analyzing the properties of local extrema after a complete rotation operation. Then, the contour of an object is identified thanks to an area correlation method. Even if this analysis of each detected contour can be time expensive, some tests made on synthetic and real images of highly overlapping coal-ash spherical particles give very satisfactory results.

The detection of elliptical bubbles has been the subject of recent papers using sophisticated image processing techniques to estimate the bubble size distribution in bubble columns (Faria et al., 2003; Honkanen et al., 2005; Fereira et al., 2012; Zhang et al., 2012; Fu and Liu, 2016; Lau et al., 2013). In order to identify a bubble on an image, the algorithms must be able to distinguish three different situations:

- (i) Single bubbles [box # 1 in Fig. 1 (a)],
- (ii) Overlapping bubbles [box # 2 in Fig. 1 (a)],
- (iii) Truncated bubbles [box # 3 in Fig. 1 (a)].

We will call single bubbles, bubbles perfectly and fully visible on the images. The edges of these bubbles do not contact the edges of other bubbles nor of the edges of the images. When two or more bubbles are superimposed on the images, the resulting object is here called overlapping bubbles. When a bubble is located at the edge of the view field, the image cannot contain all the bubble contour; these bubbles are called here truncated bubbles. Most algorithms only capture single bubbles and discard overlapping and truncated bubbles. In Faria et al. (2003), the authors develop a technique combining image analysis and discriminant factorial analysis (DFA) to classify agglomerated sucrose crystals according to their shapes. This method was adapted by Fereira et al. (2012) to study bubbly flows. Fereira et al. (2012) predict groups membership (single bubbles, medium complexity bubble groups and large complexity bubble groups) based on a combination of image descriptors (bubble area, Feret diameter, etc). However, the bubble

size distribution is evaluated using single bubbles only and the more complex groups are discarded.

For dense bubbly flows, the probability of capturing overlapping bubbles in the images increases with the bubble volume fraction and single bubbles are scarce. The statistical convergence of data could be reached by increasing the amount of images. However, this is not always possible due to experimental limitations (such as the camera's memory limit), or to extreme experimental conditions (risk of explosion for highly reactive systems, high temperatures, etc.). Furthermore, some statistical error can be suspected when a great number of bubbles is discarded. Therefore, new algorithms are necessary to increase the amount of data using a given set of images. It can be done by analyzing truncated and overlapping bubbles in addition to single bubbles. For instance, to account for the overlapping bubbles, Honkanen et al. (2005) and Lau et al. (2013) proposed two techniques: the ellipse fitting and the watershed methods. The ellipse fitting technique is based on the recognition of the connecting points of the overlapping ellipses shown in Fig. 1 (b). This method may be applied to identify highly overlapping ellipse-like bubbles. For the segmentation of overlapping bubbles, Honkanen et al. (2005) proposed to analyze the curvature of a detected contour for the detection of connecting points. Zhang et al. (2012) proposed to identify connecting points on bubble contours using a polynomial approximation of the contour shape. This last method seems to give better results than the one introduced previously by Shen et al. (2000) or Honkanen et al. (2005). The watershed method used by Lau et al. (2013) was developed by Meyer (1994) and can deal with more complex shapes by separating overlapping bubbles into individual bubbles. However, the watershed method presents two disadvantages depending on the bubble shape and its contour complexity:

- (i) The over-segmentation of objects: for instance, two overlapping bubbles separated into 3 or more objects,
- (ii) No segmentation of overlapping objects: for instance, two overlapping bubbles taken into account as a single bubble.

In Lau et al. (2013), these "segmentation errors" are quantified but solutions to overcome those problems are not suggested.

In this paper, we present a new image processing algorithm to identify bubbles within a dense bubbly flow. It accounts for truncated and overlapping bubbles in order to increase the con-

vergence of data. First, we identify in-focus bubbles with the method developed by Riboux (2007) and then used and adapted by Boulesteix (2010), Colombet et al. (2011) and Bouche et al. (2012). This method, described in Section 2.1, is based on the localization of high gradients of gray levels. Indeed, this high gradients only correspond to in-focus bubbles contour, such as the one of bubbles #5 and #6 in Fig. 1c. We have upgraded the original algorithm to detect also truncated and overlapping bubbles and to identify for each detected bubble its own membership to single, truncated or overlapping bubbles group, the objective being to apply a specific treatment technique to each group. These developments are presented in Section 2.2.

To account for the truncated bubbles, we have developed an extrapolation method in order to find the best ellipse that fits the truncated bubble contour. This method is presented in Section 2.3. The overlapping bubbles are separated using a watershed method, and a combination of the techniques used in Honkanen et al. (2005) and Lau et al. (2013). In contrast with previous works using contour curvature analysis (Pla, 1996; Honkanen et al., 2005; Zhang et al., 2012) or rotation transform analysis (Shen et al., 2000), a new method is proposed for the clear identification of connecting points. In addition, we propose a technique that prevents segmentation errors by analyzing the number of connecting points. The algorithm that we developed for these objectives is reported in Section 2.4. Note that in this work since bubble contour is close to an ellipse, this shape is used for fitting truncated bubbles. But the proposed method for segmentation can in fact be applied on any other convex object.

The overall algorithm is tested using synthetic images. The results are presented in Section 3. Finally, in Section 4, we apply our algorithm to images of air bubbles in a water/air homogeneous flow. We focus on the measurement of bubble size, shape and on the velocity variances that are very difficult to converge. Those parameters are crucial for industrial applications to evaluate dispersed phase behavior and the interfacial area, and to study the mass transfer between a liquid and a gas. By identifying more bubbles, the present algorithm is able to extract longer trajectories with a tracking particle method based on the comparison of bubble center positions between consecutive images. The latter is very important to accurately determine the bubbles dynamic in the swarm.

2. Image processing algorithm

The purpose of this algorithm is to distinguish the bubbles from the background in gray-scale images to determine their size, shape and by following their position through successive images to determine their trajectory and to measure their instantaneous velocities. The algorithm is based on the the 'First version algorithm' developed by Riboux (2007) and adapted by Boulesteix (2010), Colombet et al. (2011) and Bouche et al. (2012). It is devoted to capture single bubbles in gray level images using a gradient method. Since single bubbles are scarce in dense bubbly flows, the challenge is here to upgrade this algorithm to account for truncated and overlapping bubbles. Therefore, given a set of images, a faster convergence of data could be achieved by capturing truncated and overlapping bubbles in addition to single bubbles.

The squeleton of the original algorithm is briefly presented in Section 2.1. In Section 2.2, we describe the novel developments to determine to which group each detected object belongs (single, truncated or overlapping bubbles group as defined in the introduction). Then, the algorithms that we have developed to account for truncated and overlapping bubbles are presented in Sections 2.3 and 2.4.

2.1. The first version algorithm

The first version algorithm presented in this section was initially developed to measure accurately the bubble size by detecting only in focus bubbles. Indeed, the apparent size of a bubble outside the focal plane is changed by the field angle of the lens. Therefore, discarding out-of-focus bubbles allows a better accuracy in the measurements of the bubble size and shape. Let us notice that with commonly-used threshold selection methods such as the algorithm of Otsu (1979), most of the bubbles from the gray-scale images are identified but bubbles in and out of focus are indistinguishable. The algorithm identifies in-focus bubbles by computing gradients of gray-levels, because high gradients only correspond to in focus bubble contours. The following strategy is applied:

1. The gray-level gradient of raw images such as the image in Fig. 2a, is computed with a σ filter developed by Marmottant (2001). The operation result is reported in Fig. 2b. The σ filter has been selected because, unlike commonly-used filters (such as the Roberts, 1965; Sobel, 1970 or Prewitt, 1970 filters) which can exhibit significant anisotropic behavior, the σ filter has a more isotropic property. It is defined as follow:

$$\sigma = \sqrt{\langle (N - \langle N \rangle)^2 \rangle} \tag{1}$$

$$\langle N \rangle = \frac{1}{8} \left(N \otimes \begin{pmatrix} 1 & 1 & 1 \\ 1 & 0 & 1 \\ 1 & 1 & 1 \end{pmatrix} \right) \tag{2}$$

where $N(m, n)$ is the pixel-matrix corresponding to the gray-level image of dimensions $m \times n$. $\otimes$ is the convolution operator so that $< N(m, n) >$ returns the averaged value of the height pixels around a pixel at a given position (m, n) in the original image (resulting in the prefactor 1/8 in Eq. (2)). Then, the final result is the matrix $\sigma(m, n)$ corresponding to the calculation of standard deviation between the height neighboring pixels. The operator $\langle - \rangle$ in Eq. (1) is the arithmetic average. This filter enables an estimation of the mean gray level gradient intensity considering thus the 8 directions around one pixel, which supply a better isotropic behavior than conventional filters. To get more informations on that filter and on its behavior, the reader can refer to Marmottant (2001) (p. 52–56).

2. High gradients of gray-levels above a user-defined threshold T_{hg} are identified in Fig. 2b. The threshold T_{hg} is determined by dichotomy using an image where bubbles out and in the depth of field must be distinguished. For instance, in Fig. 1c, the threshold T_{hg} can be chosen to keep objects #5 and #6 and discard objects #1, #2, #3 and #4.

3. Closed contours of selected objects are subsequently filled in, as depicted in Fig. 2c.

4. To deal with measurement noise, small objects under a second user-defined threshold T_{ss} are filtered (cf Fig. 2d). This threshold is a small fraction of the projected area of a bubble estimated using the average equivalent diameter $\tilde{D}_{eq}$: $T_{ss} \sim 0.08 \, (\pi \, \tilde{D}_{eq}^2/4)$

5. Objects at the image edges are discarded since they may be truncated bubbles.

6. To avoid detecting overlapping bubbles, only the convex objects are kept by the algorithm and identified as bubbles (Fig. 2e). The "solidity" property S of a detected object Ω, defined as the ratio of the object area to its convex hull area, is used to discriminate concave objects with a solidity property S under a third user-defined threshold T_S such as T_S is close to unity. In the present study as in the version used by Colombet et al. (2011), T_S is fixed to 0.98.
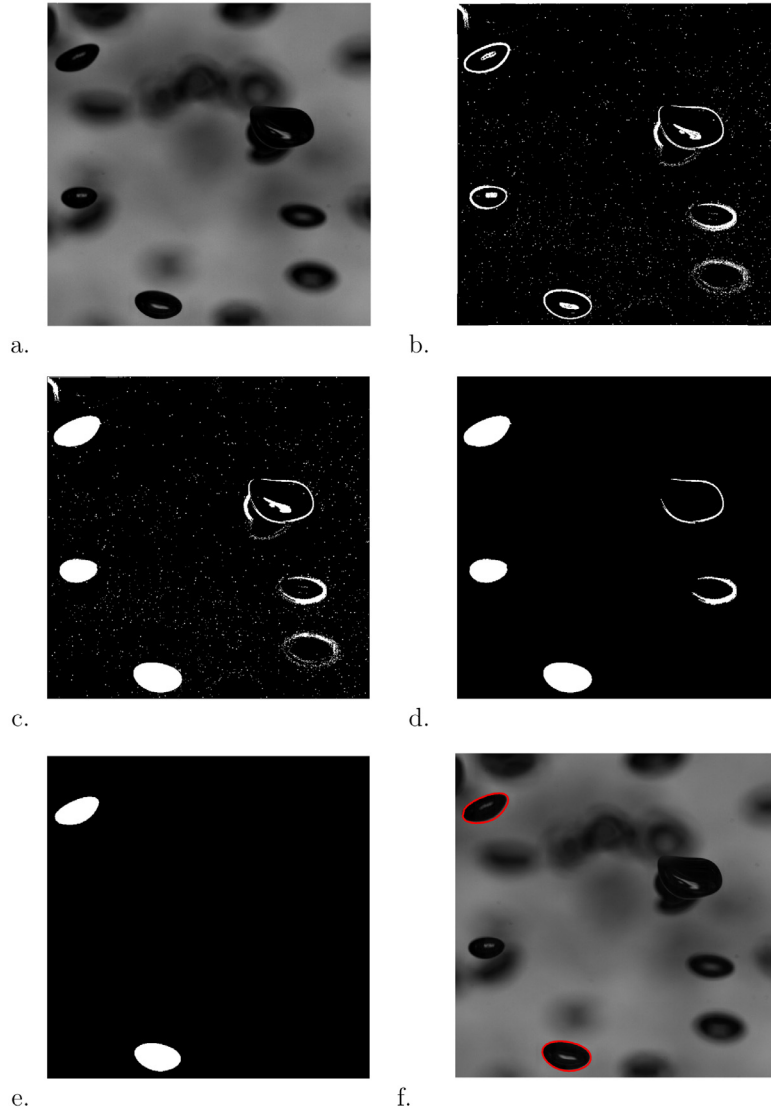
Fig. 2. Image segmentation with the gradient method: (a) gray-level raw image from Colombet et al. (2011), (b) binarisation applying the threshold T_{hg} on the gray-level gradient image, (c) filling of objects having a close contour, (d) small objects corresponding to noise are discarded applying the threshold T_{ss} on objects area, (e) only convex objects are then kept by applying the threshold T_S on objects "solidity" property, (f) final result with raw image and bubble detection denoted by a red line. (For interpretation of the references to color in this figure legend, the reader is referred to the web version of this article.)

Table 1
Elliptical regression test case on a single perfect ellipsoidal object: ratio of the surface area of the extrapolated ellipse S_{ee} to the surface area of the initial ellipse S_0 versus the percentage of the contour used for the regression.

% of the ellipse contour	100	60	40	10	7	5	4
S_{ee}/S_0 in %	$< 10^{-16}$	$< 10^{-16}$	$< 10^{-16}$	10^{-16}	0.0012	0.12	2.72

The final result is shown using a red line in Fig. 2f. This image processing algorithm can identify in focus single bubbles in gray level images. However, by applying this method to detect bubbles in complex images with high void fractions, this first version algorithm is unable to detect enough bubbles to achieve a good statistical data convergence with a reasonable number of processed images because a large number of bubbles are truncated and/or overlapping bubbles and are not accounted for. New developments were performed in order to detect more bubbles from the images by taking truncated and/or overlapping bubbles into account. In the following section these new developments allowing to detect these special situations and to predict group memberships are presented (single, truncated or overlapping bubbles).

2.2. Group membership prediction

The original algorithm is modified to determine if the detected object is a single, truncated or overlapping bubble using the following strategy:

• **Single bubble:** If the detected object meets the criteria 1–6 presented in Section 2.1, it corresponds to a single bubble.

• **Truncated bubble:** If the detected object does not meet criterium 5 but does meet criterium 6 (Section 2.1), it corresponds
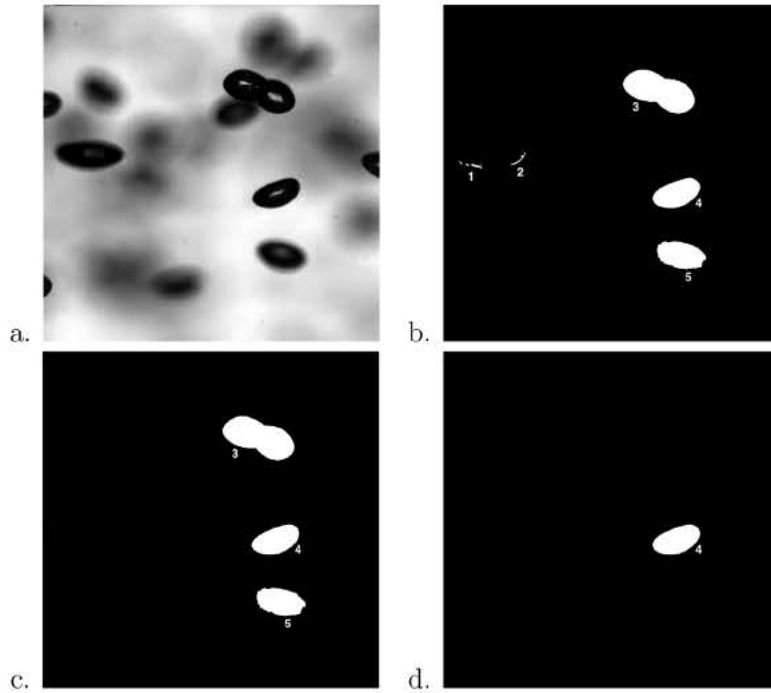
Fig. 3. Image segmentation of image (a) with the gray level gradient method for three different "solidity thresholds": $T_S = 0$ (b), $T_S = 0.50$ (c) and $T_S = 0.95$ (d).
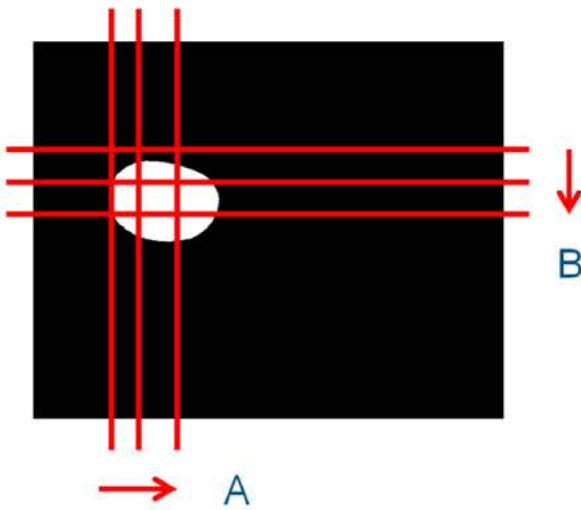

Fig. 4. Test n°2 of the truncated bubble treatment: Vertical (A) and horizontal (B) truncation of a binary image of a real bubble.

Fig. 5. Test n°2 of the truncated bubble treatment: S_{ee}/S_b as a function of the dimensionless surface area of the truncated real bubble S_{tb}/S_b.

to a single truncated bubble (convex object) located at an image edge.

- **Overlapping bubbles:** The solidity threshold T_S (criterium 6, Section 2.1) determines which object is considered "concave enough" to be a single ellipse-like bubble. Fig. 3 shows that the detected objects shape depend on the values of T_S. On the one hand, a small value of T_S results on the detection of pieces of bubble contours (such as objects #1 and #2 in Fig. 3b), overlapping bubbles (object # 3 in Fig. 3b) and deformed bubbles (object #5 in Fig. 3b). On the other hand, a higher value of T_S allows detecting single bubbles only (object #4 Fig. 3d). Therefore, in this investigation, we choose a threshold $T_S = 0.98$. If the detected object does not meet criterium 6 (Section 2.1), there is a possibility that it corresponds to overlapping bubbles. To avoid detecting pieces of bubble contours, an another threshold T_{S2} is defined to discard objects

with a solidity property S below T_{S2}. In this study T_{S2} is close to 0.8. In addition, we must account for other criteria:

- Is the object surface area significantly higher than the average surface area given by the statistic from the detection of single bubbles?
- Are there some inflection points in the detected object? An inflection point (also called 'breakpoints' or 'connecting points' in some other works) refers here to a point along the object contour where the contour curve crosses its tangent. Since bubble shape are ellipsoid, the presence of two inflection points along the contour indicates that the detected object corresponds to two overlapping bubbles.

If the answer to the two questions above is yes, then the detected object corresponds to overlapping bubbles. Let us notice that overlapping bubbles can also be truncated bubbles that do not meet criterium 5.

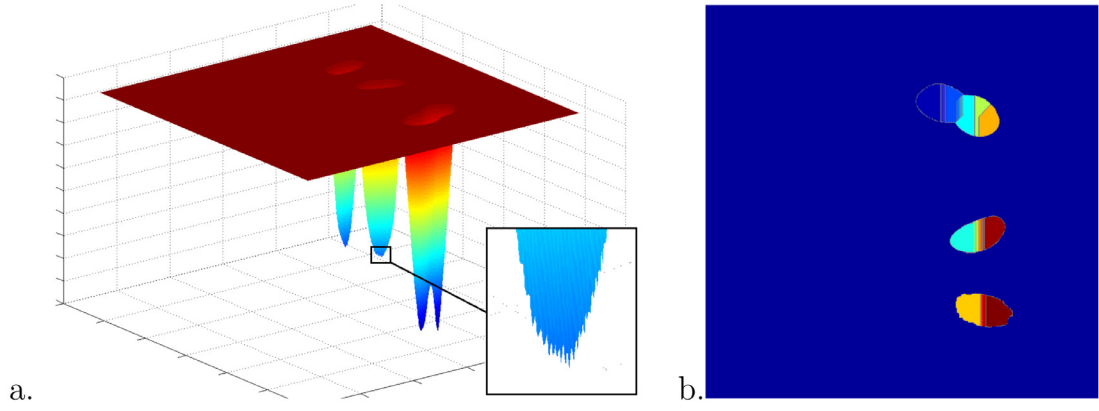**Fig. 6.** (a) Euclidean distance map of the binary image 3c and local minima of the distance map. (b) Over-segmentation of detected objects in 3c using the watershed algorithm of Meyer (1994) and the distance map in (a).
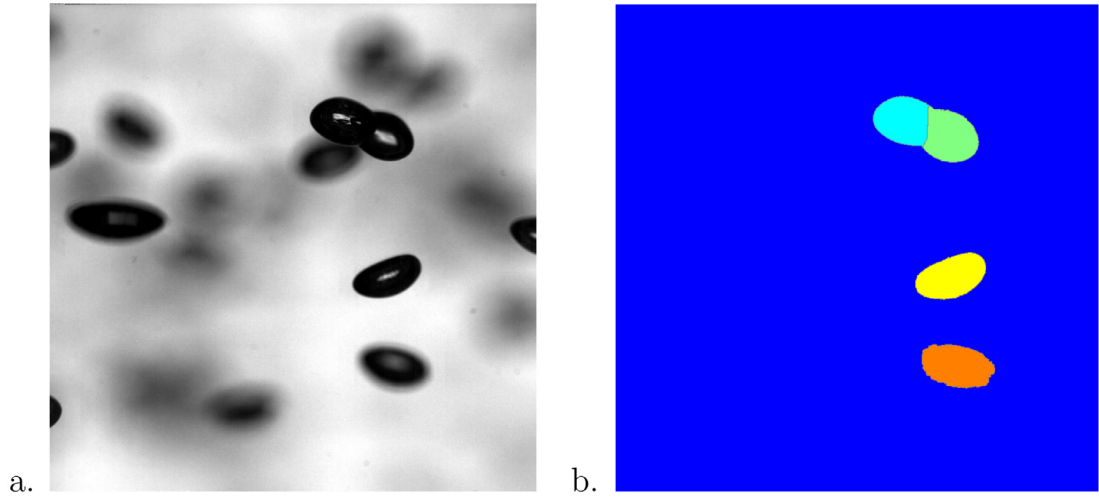

Fig. 7. Watershed segmentation using a distance map filtered by *medfilt2 Matlab®*. The detected objects are previously transformed using morphological operations (erosion and dilatation).

2.3. Truncated bubbles treatment

In the following, a truncated bubble refers to a bubble, located at the edge of an image, cut because partially out of the field of view. Truncated bubbles are approximated by an ellipse because it is the classical bubble shape observed in bubbly flow for a wide range of bubble sizes and physical properties. As reported by Clift et al. (1978), this shape applies particularly well in bubbly flows characterized by a low Bond number as $Bo = \Delta \rho$ g D_{eq^2}/σ considered in Section 4 ($Bo < 1$).

Therefore, the purpose of the treatment is to find the ellipse that best fits the truncated bubble contour points. The first step is to locate the bubble contour points, which are the coordinates of the contour pixels. Then, the canonical equation coefficients of the best fitting ellipse are computed with a full least squares method proposed by Halíř and Flusser (1998). This method, also used by Zhang et al. (2012), is chosen for its robustness and efficiency.

Its performance is estimated with two tests. The first test concerns the elliptical regression on a truncated contours of a perfect ellipse. For this first test, we have consider an initial ellipse that is defined by the following equation:

$$\frac{x^2}{b^2} + \frac{y^2}{a^2} = 1 \tag{3}$$

where x and y are the ellipse cartesian coordinates in the system defined by the bubble center and the semi-axis unit vectors. For this test case on synthetic images, the aspect ratio $\chi = b/a$ has been fixed to be close to the one typically observed in a bubbly flow, with $\chi = 2$. For this purpose, the semi-axis are fixed to be $a = 2$ mm and $b = 4$ mm, x and y being also expressed in mm.

One hundred points are uniformly distributed on the ellipse contour and the elliptical regression algorithm is applied using a limited number of consecutive points to simulate the regression of a truncated ellipse. The number of consecutive contour points is varied from 5 to 100. The extrapolation error is estimated using the ratio of the surface area of the extrapolated ellipse S_{ee} to the surface area of the initial ellipse S_0. The results are reported in Table 1. This test shows that over 10 points (10% of the contour line) the extrapolated ellipse perfectly fits the initial ellipse (relative error $< 10^{-16}$ on the surface area). This test case highlights that the algorithm is very effective and convergent for ideal ellipses since the resulting points perfectly fit the contour and the regression doesn't need a large amount of contour points. This method is a perfect candidate for fitting the contour of highly truncated bubbles.

The second test is the elliptical regression of a gradually truncated binary image of a real bubble. Two truncations directions are tested. They are shown in Fig. 4. This test case is more difficult than the previous one because 2D images of real bubbles are not ideal ellipses. The truncation is first performed from left to right (vertical truncation, A) and then, another truncation from top to bottom (horizontal truncation, B) is independently performed. As
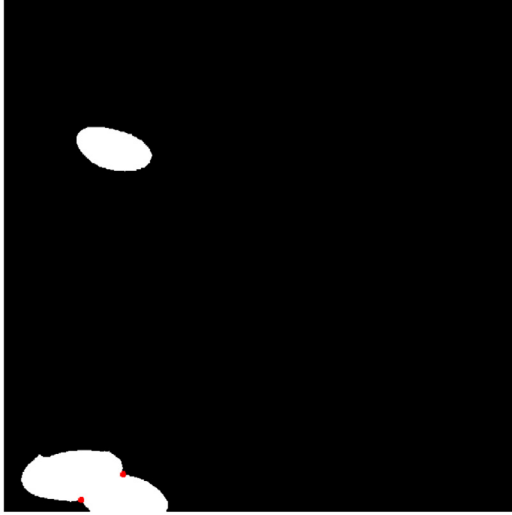
Fig. 8. Binary image of a single bubble and an overlapping bubble. The red points are the inflection points.(For interpretation of the references to color in this figure legend, the reader is referred to the web version of this article.)
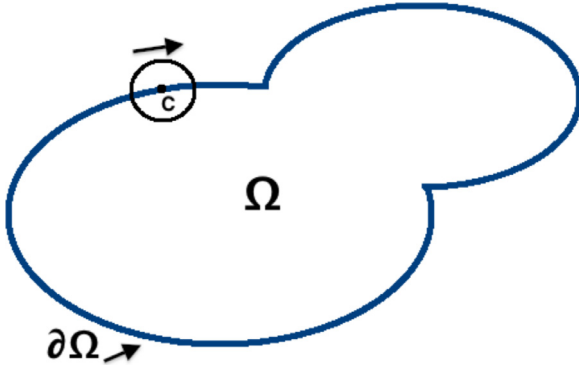

Fig. 9. Illustration of the algorithm used to locate inflexion points on the contour of an object Ω.

Table 2
Ellipses properties range for the set of synthetic images.

	Lower bound	Upper bound	Unit
X_0	−25	1310	pixels
Y_0	−20	1074	pixels
Major axis	200	300	pixels
Minor axis	100	200	pixels
Angle	$-\pi/8$	$\pi/8$	rad

for the first test case, the fitting error is defined as the ratio of the extrapolated ellipse surface S_{ee} to the initial bubble surface S_b. It is reported in Fig. 5 versus the dimensionless surface area of the bubble after truncation S_{tb} (truncated bubble area). Whatever the truncation direction (A or B) the figure shows that the extrapolation error remains under 10% if the surface area S_{tb} is higher than 50% of the initial bubble surface area S_b. Therefore, in order to add only relevant data to statistics, only truncated bubbles with surface area above a threshold corresponding to a surface ratio $S_{tb}/S_b \geq 50\%$ will be extrapolated. Since whole surface area of a truncated bubble is unknown, this threshold is taken as 50% of the average surface area of single bubbles $\tilde{S}_b$ previously computed after a first data processing with a sufficient number of images.

2.4. Overlapping bubbles treatment

Fig. 3 shows that to avoid detecting overlapping bubbles and pieces of bubble interfaces (objects #1 and #2), a restrictive solidity threshold is necessary discarding as a consequence a large number of overlapping bubbles when the void fraction increases. Thus, we have developed an image processing algorithm that can: (i) identify the objects corresponding to overlapping bubbles and, (ii) separate and reconstruct these overlapping bubbles. In this section we focus on point (ii), point (i) being presented in section 2.2.

2.4.1. The basic watershed method

The method commonly used to separate mostly convex overlapping objects is the watershed segmentation, proposed by Beucher and Lantejoul (1979) and Lantejoul and Beucher (1981). The purpose is to build boundaries between objects with the following strategy:

• First, the Euclidean distance map of the binary image is computed. The result is a matrix in which each coefficient corresponds to a pixel of the binary image. It can be interpreted as a physical elevation as shown in Fig. 6a. The coefficients corresponding to black pixels are equal to 0. The ones corresponding to white pixels next to the object contours are equal to −1. The value of the other coefficients depend on the shortest distance to the contour.

• To build the boundaries separating overlapping bubbles, let us imagine water sources feeding each local minimum of the relief in Fig. 6a. Lakes with increasing water level are so created. A separating "vertical wall" is built whenever different lakes meet each other. This wall define the line separating the overlapping objects.

2.4.2. First treatment of over-segmentation problems

The watershed segmentation of the binary image 3c is shown in Fig. 6b where each separated object has a different color. It was performed using the watershed algorithm of *Matlab®* based on the work of Meyer (1994). The figure shows that the use of the algorithm in that case leads to the over-segmentation of the object. This is due to the presence of small local minima on the Euclidean distant map (Fig. 6b) because the contours are not always perfectly defined at the pixel scale. To overcome this problem, the following solutions were tested:

• To smooth the distance map and remove the local minima, morphological operations (erosion, dilatation, opening and closing) can be applied on the object areas of the detected overlapping bubbles. We have tested an opening morphological operation (erode-dilate). The structuring element was a 3 pixels in radius disc. The operation reduced the number of fragments but not enough to overcome the whole problem.

• The distant map was then filtered with the *Matlab®* function *medfilt2* using a 3-by-3 neighborhood pixels matrix. Since it is a low-pass filter, it allows filtering the local minima corresponding to high frequencies of the distance map, decreasing their number, so also the number of lakes used for the watershed technique. The operation leads to much more satisfactory results shown in Fig. 7. This filtering technique has so been selected.

2.4.3. Supplementary treatment of over-segmentation problems

In some cases, despite all the previous operations, the watershed segmentation is not able to properly separate the overlapping bubbles. The corresponding objects have to be discarded from the analysis in order to keep the quality of the statistical results. The challenge here, is to determine whether or not the segmentation is properly performed, by locating the contour inflection points. Indeed, if a contour has one (or more) inflection point(s) there are at least two overlapping bubbles. For instance, Fig. 8 shows the object contour inflection points (red dots) corresponding to the connection points of the two bubbles.
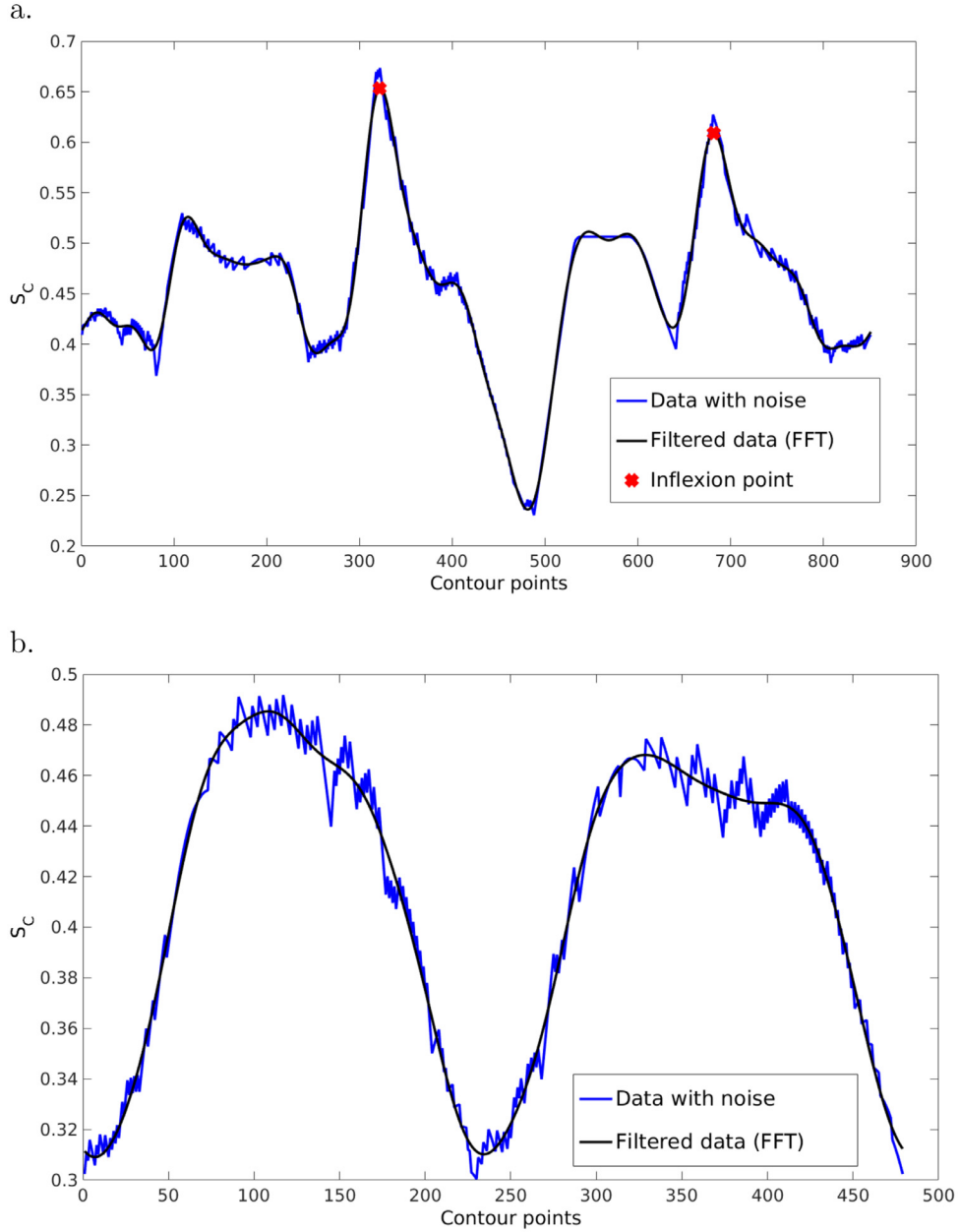
a.

b.

Fig. 10. The ratio S_C for every pixel of the contour (▬▬▬); filtered data with a Fast Fourier Transform (—) and detected inflexion points (●) are reported in (a) for the overlapping bubbles in the lower left corner of Fig. 8 and in (b) for the single bubble in the upper left corner of the same figure.

One method to locate the inflection points is to compute the curvature at each point of the object interface. The inflection points correspond to the peaks of the curvature. However, the resulting signal often includes a lot of noise. As a consequence, it is quite difficult to automatically identify the peaks corresponding to actual inflection points. Therefore, another original and more robust method was developed.

Let us define a disk D of radius R and center C. When the disk center moves along the boundary $\partial\Omega$ of the detected object Ω, like in Fig. 9, the dimensionless area of the intersection of the disk and Ω is defined as follows:

$$S_C = A(D \cap \Omega)/A(D) \qquad (4)$$

where $A(D)$ is the area of D. S_C can vary from 0 to 1. The shape of the object is characterized by plotting the area S_C along $\partial\Omega$. High frequencies of this signal are filtered with a Fast Fourier Transform (FFT) using an empirical frequency-threshold that depends on image quality and sharpness of bubble contour. In this work, signal

frequency higher that 0.2 Hz are removed. Then, the peaks are determined by analyzing the sign of the derivative. Inflection points correspond to the peaks C_i where S_C is above a coefficient η such as $0.5 < \eta < 1$.

One can note that the use of FFT has been also employed by Honkanen et al. (2005) to erase noise from the contour of bubbles. In our case, it is applied not directly on a bubble contour but on the surface ratio S_C.

The coefficient η may depend on the radius of the disk and the quality of images. In Fig. 10a, with a coefficient $\eta = 0.6$, the algorithm is able to determine the two inflection points for the object detected at the lower left corner in Fig. 8 that correspond to the two connection points of the overlapping bubbles. For the object detected at the down left corner in Fig. 8, the Fig. 10b shows that S_C is smaller than η for all the peaks C_j which corresponds to a single bubble. Therefore, the algorithm is also able to distinguish single and overlapping bubbles.
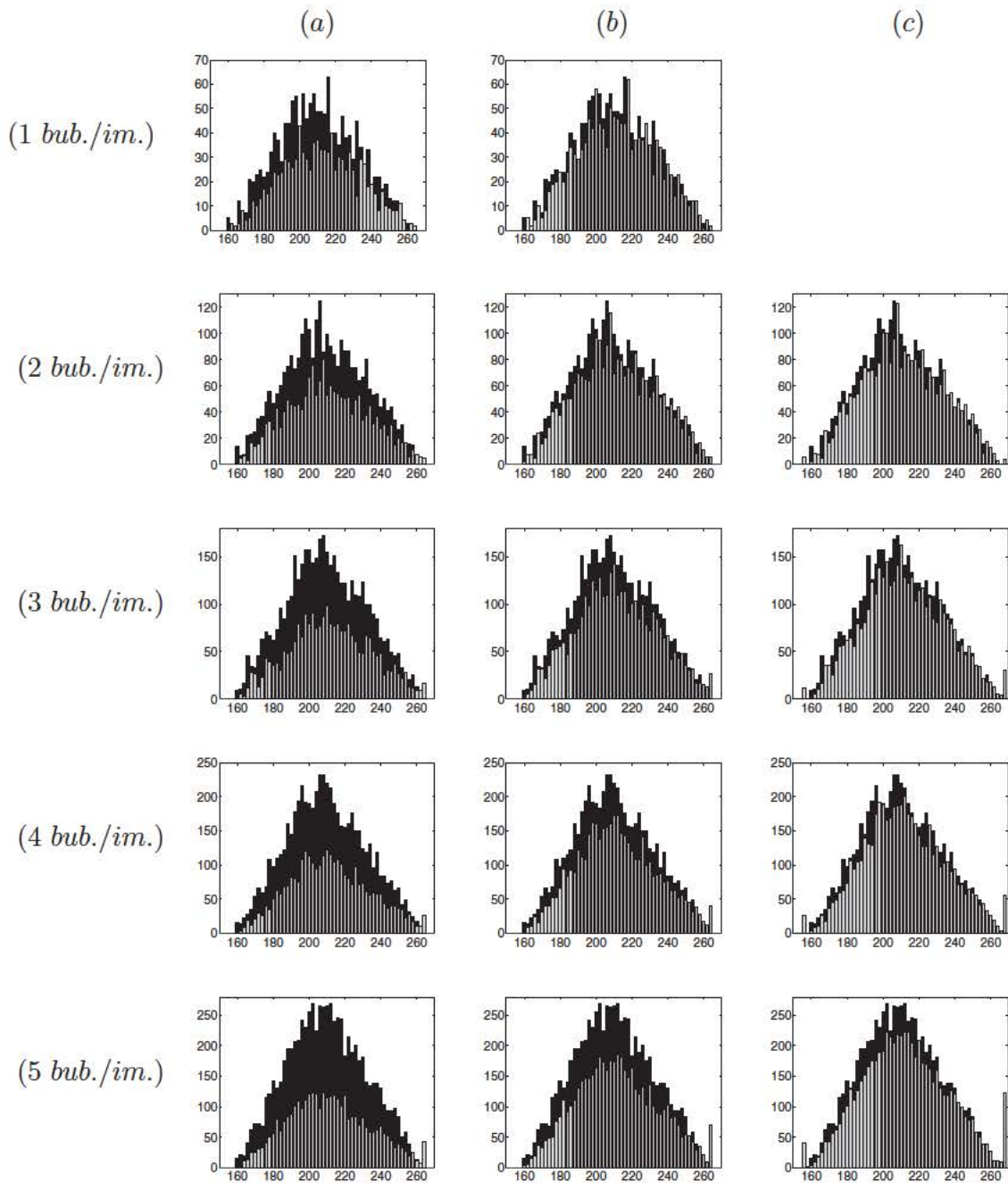
Fig. 11. Histogram comparison of bubble volume equivalent diameter for synthetic images with different number of bubbles per images: black histogram = theoretical bubble distribution, gray histogram = histogram from image processing with the detection of (a) single bubbles only; (b) single and truncated bubbles; (c) single, truncated and overlapping bubbles.

2.4.4. Overview of the overlapping bubbles treatment

The new method to deal with overlapping bubbles can be described as follows:

1. If the "solidity" S of a detected object Ω is between T_S and T_{S2}, where T_S is the solidity threshold for single bubbles and T_{S2} is another user-defined threshold such that $T_{S2} < T_S$, the object is assumed to correspond to overlapping bubbles. In the present study, $T_S = 0.98$ and $T_{S2} = 0.8$.
2. The opening morphological operation is applied on the object Ω.
3. The distance map is computed and filtered using *medfilt2* (Matlab®).

4. The watershed algorithm is applied on Ω, which is separated into N_S parts.
5. The inflection points of Ω contour are determined.
6. If the number of inflection points is strictly higher than the number of parts N_S, the object Ω is discarded.
7. If not, the contour of each part of Ω is extracted and an elliptical regression identical to the one developed for truncated bubbles is performed for each one.

Note that by applying the point 6, in this treatment, clusters composed of a long chain of overlapping bubbles are discarded and one focuses on the segmentation of compact bubbles clusters of 1,2 or 3 objects that are usually found in dense dispersed flows.
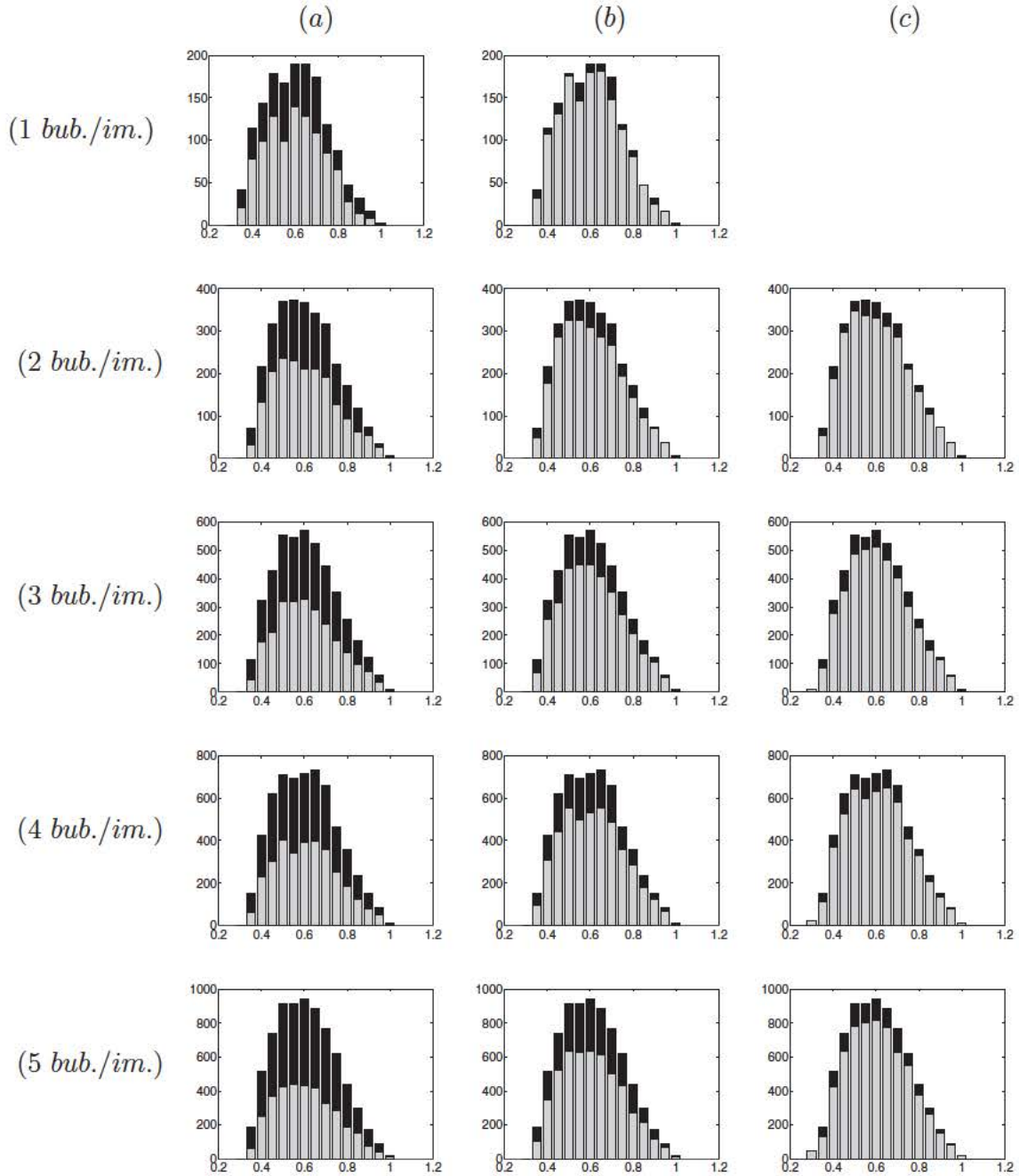
Fig. 12. Histogram comparison of bubble axis ratio (small axis/ large axis) for synthetic images with different number of bubbles per images: black histogram = theoretical bubble distribution, gray histogram = histogram from image processing with the detection of (a) single bubbles only; (b) single and truncated bubbles; (c) single, truncated and overlapping bubbles.

2.5. The new image processing algorithm

As detailed in the previous sections, the initial image processing algorithm has been modified in order to extract more bubbles. The whole image analysis process is a robust method that can account for truncated bubbles (Section 2.3) and overlapping bubbles (Section 2.4). The global strategy of the new algorithm is summarized as follows:

1. Computation of the gray-level gradient fields for the raw images with the σ filter;
2. Identification of high gradients of gray levels above a threshold T_{hg} to find in focus bubble contours;
3. Fill in all the closed contours;

4. Erasing image noise by discarding smallest objects below a user-defined threshold T_{ss};
5. Identification of single bubbles, truncated bubbles and overlapping bubbles (see Section 2.2);
6. Creation of a set (Set A) of binary images keeping on the images single bubbles, and truncated bubbles with a surface area higher than 50% of the average single bubble surface area. Simultaneously, creation of another set (Set B) of binary images containing only the overlapping bubbles. The sets A and B are then treated in different ways;
7. For set A, elliptical regression of truncated bubbles using their contour points (Section 2.3) and then extraction of all the bub-

Table 3

Test on synthetic images: number of captured ellipses and percentage of single, truncated and overlapping objects as a function of α.

Ellipses per image	1	2	3	4	5
α (%)	5.65	4.28	5.75	7.25	9.33
Number of captured ellipses	1266	2415	3790	4669	6446
Single objects (%)	71.0%	66.7%	59.7%	59.4%	48%
Truncated objects (%)	29.0%	28.5%	31.7%	25.7%	31.7%
Overlapping objects (%)	0%	4.8%	8.6%	14.9%	19.6%
Total captured ellipses (%)	84.4%	80.5%	84.2%	77.8%	85.9%
Ratio (Truncated + Overlapping)/Single	0.41	0.50	0.67	0.68	1.08

Table 4

Air/water system properties at $T = 20^oC$ and $P_{atm} = 101,325$ Pa.

Name	Notation	Unit	Value
Liquid Density	ρ_L	kg m^{-3}	998.2
Gas Density	ρ_G	kg m^{-3}	1.2
Liquid Viscosity	μ_L	Pa s	1.002×10^{-3}
Gas Viscosity	μ_G	Pa s	18×10^{-6}
Surface tension	σ	N m^{-1}	0.073
Molar fraction (in dry air)	x_{O_2}		20.9%
Molar fraction (in dry air)	x_{N_2}		79.1%

bles geometrical parameters (surface area, volume, centroid, minor and major axis,...);

8. For set B, application of the seven image processing steps developed for the overlapping bubbles (see Section 2.4) and then extraction of all the bubbles geometrical parameters as previously done for set A;

9. Gathering the results for set A and B.

The threshold on gray level gradient T_{hg} depends on the camera sensitivity, but it can be estimated automatically from the histogram of the gradient image intensity. For erasing small objects due to image noise, the threshold T_{ss} that corresponds to 8% of the mean surface object is quite general and shouldn't depend on the flow if the population of bubbles is not too widely dispersed in size. But, if the population is very poly-dispersed, this threshold needs to correspond to a small fraction of the smallest bubbles one needs to detect. The chosen thresholds to keep only single bubbles $T_s = 0.98$, to detect overlapping bubbles $T_{s2} = 0.80$, as well as the threshold on surface ratio $50\% \tilde{S_b}$ to make ellipse regression seem to be very robust.

3. Test on synthetic images

In order to test the image processing methods described in the previous sections, synthetic binary images of ellipses were used. The ellipses were randomly generated by the definition of the center, the major and minor axes and the angle between the x-axis and the major axis of the ellipse. The ranges of these parameters are reported in Table 2. They were chosen to be close to the parameters on images of real rising bubbles. The image size for synthetic test was 1285×1024 pixels. Single bubbles, truncated bubbles as well as overlapping bubbles are randomly created on these synthetic images. Five series of 1500 images (with 1, 2, 3, 4 and 5 ellipses per image) were generated in order to study the influence of the void fraction α on the performance of the image processing methods.

The results are summarized in Table 3. The second line of this table presents the variation of the average value of the gas fraction α when the number of ellipses per image varies (first line). α is here calculated in 2D from the synthetic images. The tests were performed from $\alpha = 5.65\%$ to $\alpha = 9.33\%$, a relevant range value for bubbly flows. The global number of captured ellipses increases

from 1266 to 6446 as the number of ellipses per image increases from 1 to 5 i.e. when the void fraction increases.

The three following lines of Table 3 present in detail the distribution of single, truncated and overlapping objects among the captured objects. At low void fraction (1 ellipse per image), 29% of the captured objects are truncated ones (located on the edge of the images). These objects were not captured and accounted for by the initial image processing technique. When the void fraction increases, the percentage of single objects decreases from 71% at $\alpha = 5.65\%$ to around 50% at $\alpha = 9.33\%$, meaning that the proposed image processing captures twice the number of objects captured before the developed treatments of truncated and overlapping objects.

The two last lines of Table 3 enable to appreciate the real efficiency of the new image processing. When the number of bubbles per images increases (i.e. when increasing the void fraction), the percentage of total captured bubbles remains quite stable between 77 and 86% despite the significant increase of truncated and overlapping bubbles. The ratio between the number of truncated and overlapping detected bubbles on the number of single detected bubbles (last line of Table 3) increases significantly from 0.41 to 1.08 when increasing the gas fraction.

Figs. 11 and 12 report the histogram of equivalent diameter and bubble axis ratio respectively. In those two figures, the histogram corresponding to the bubble population imposed in synthetic images is plotted in black and the histogram of detected bubbles is plotted in gray. From top to bottom, the number of bubbles per image is increased and from left to right the following three cases are considered :(a) only single detected bubbles, (b) single and truncated detected bubbles, (c) single, truncated and overlapping detected bubbles. Note that there is no figure (c) at the right hand top corner because it is not possible to get overlapping bubbles when imposing one bubble per image.

In Fig. 11, in agreement with statistics reported in Table 3, for a given treatment (a, b or c), when displacing vertically, the increase of the number of bubbles per image generates a larger difference between the histogram from image treatment and the original one. This is due to the fact that the number of no detected bubbles increases with the number of bubbles per image. But fortunately in the same time, for a given number of bubbles per image, when displacing on the right and adding the detection of truncated and then overlapping bubbles, we can easily observe that the histogram get closer and closer to the original histogram. This improvement of bubble size measurement is a consequence of the significant increase of detected bubbles. The same behavior is found in Fig. 12 concerning the measurement of the histogram of bubble axis ratio. In addition, in both figures, the filling of classes is performed homogeneously in all the classes, showing that the treatment is bubble size independent. Thus, the added value of the main steps of the process is clearly shown in Figs. 11 and 12.

However, some drawback of overestimations located specifically at the boundary of histograms can be pointed out. Concerning bubble size histogram measurements, in Fig. 11, if we consider figure
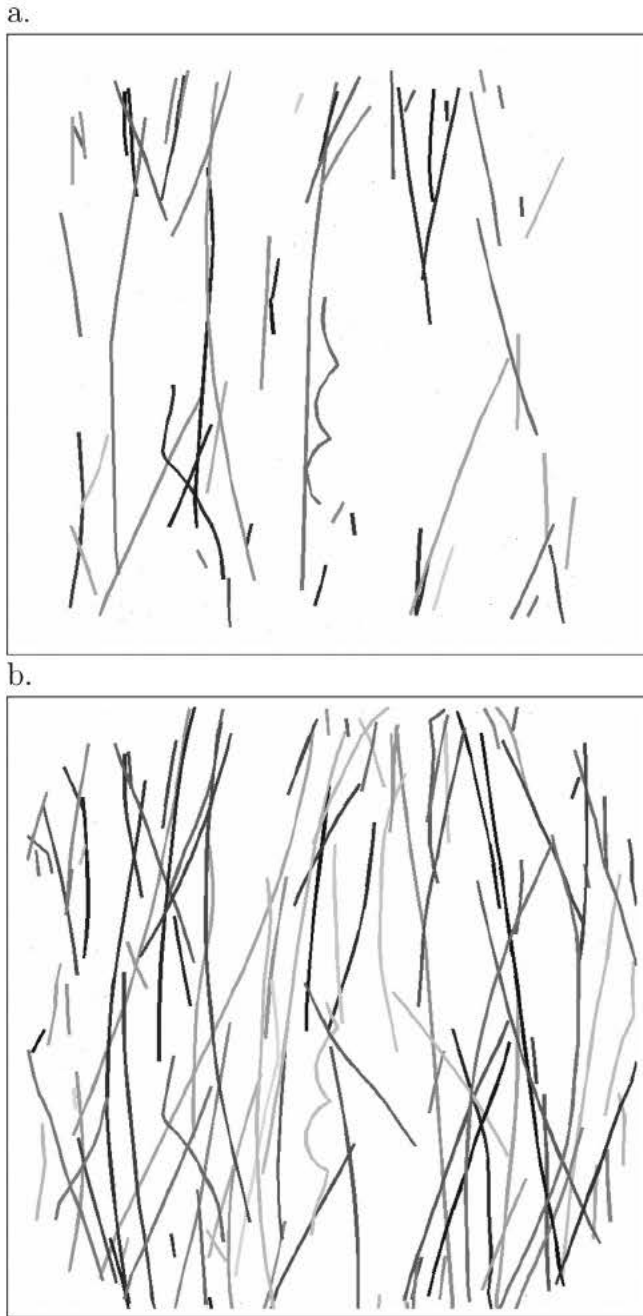
a.

b.

Fig. 13. Trajectories of bubbles for a reduced set of 1500 images with $\alpha = 0.5\%$. (a) Detection of single bubbles only (algorithm used by Colombet et al., 2011). (b) Detection of single, truncated and overlapping bubbles (present new algorithm).

Fig. 14. Variances of vertical (z) and horizontal (x) bubble velocity against gas volume fraction α. ($\triangledown$) $V(V_z)$ Optical probe by Riboux et al. (2010), ($\diamond$) $V(V_x)$ and ($*$)$V(V_z)$ by Colombet et al. (2015), ($\square$) $V(V_x)$ and ($\circ$) $V(V_z)$ from present work.

3-4-5 bubbles per image, we could see the birth of a class of small axis ratio. But globally, the histogram of axis ratio is not drastically affected by the appearance of large or small bubbles size classes that are reported in Fig. 11.

As these overestimations mainly appear out of the range of the histogram, a simple filter could be added to remove these artifacts and so only consider relevant data. This filter has not been applied here to show the complete behavior of the image treatment, but it could be easily implemented by users. The good results obtained here with synthetic images clearly demonstrates the capability of the proposed image processing technique to improve particle size and shape measurement in dispersed flows. In the following section, this approach is applied on experimental data for a bubbly flow in a air/water system.

4. Application to an air/water bubbly flow

4.1. Experimental set-up

Air bubbles rising in water at ambient temperature and pressure are investigated in this section. The experimental set-up that provided the images has also been used by Riboux et al. (2010) and Colombet et al. (2011, 2015). The reader can refer to Colombet et al. (2015) to get a schematic but detailed description of the experimental set-up. Air bubbles are injected in a square section glass column ($15 \times 15 \times 100$ cm^3) using three different flow meters in order to vary the gas flow rates and the gas volume fraction. A series of 841 capillaries of 15 cm long and inner diameter $d_i = 0.2$ mm covering the whole column section generates a bubble swarm that has been verified to be homogeneous. The column was filled in with filtered tap water (particles larger than 15 μm were removed) and Colombet (2012) have shown that the phase system can be considered to be close to a clean system. The properties of the fluids are reported in Table 4 where the subscript L refers to the liquid (water) and the subscript G for the gas (air). In addition, as already reported by Duineveld (1995) or Ellingsen and Risso (2001), the bubble shape of air bubble in water remains close to the one of an oblate ellipsoid as long as the volume equivalent diameter remains lower than 2.5 mm as in present experiments.

The images were taken with a high speed CMOS camera (*Photron APX*) with a 105 mm fixed-focus lens (*Nikon*). The camera was positioned horizontally, aligned with the center of the column, at a distance of 150 mm from the injectors and in order to visual-

(a) for 3-4-5 bubbles per image, we can first notice the formation of a class of large bubbles that is due to the detection of slightly overlapping bubbles considered as single bubbles. This default is directly link to the severity given to the threshold T_S on bubble "solidity". Then if we consider the passage from figure (a) to figure (b) or from figure (b) to figure (c) some defaults in detection of truncated and overlapping bubbles generate also an increase of this class corresponding to largest bubbles. Similarly, we can observe the appearance of a class of small bubbles when passing from figure (b) to (c) and adding the detection of overlapping bubbles. This phenomena is typically causes by default in bubble splitting leading to some over-segmentation cases generating small objects. In Fig. 12, if we consider the passage from figure (b) to figure (c) for
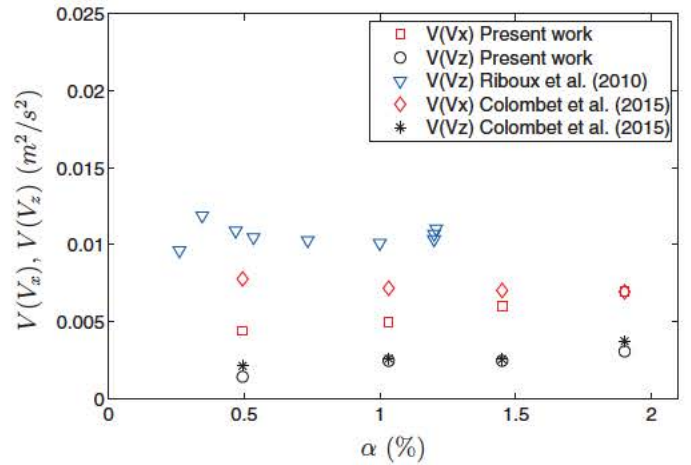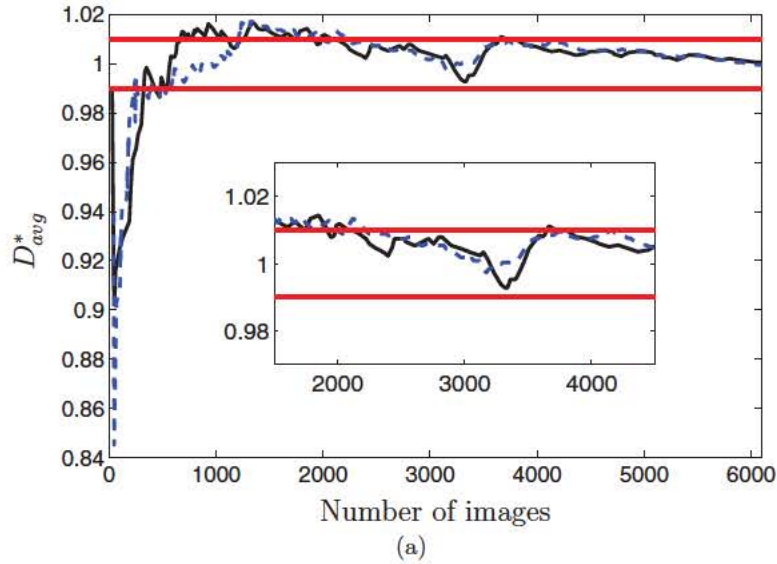
Fig. 15. Dimensionless average equivalent diameter D_{avg}^* versus the number of images Ni. (–) Original algorithm used by Colombet et al. (2011), (– –) present algorithm, red lines correspond to a measurement convergence of $\pm 1\%$.

ize a field located at 15 mm from the glass wall inside the bubbly flow. The depth of field is 0.8 mm with a lens aperture of f/2.8. The acquisition frequency is 500 images/s and the dimensions of the view field are 18×18 mm^2 with a resolution of 56.8 px/mm. Two systems were used to provide light, depending on the gas volume fraction. A 100×100 mm^2 LED backlight of 65.700 cd/m^2 was used for low gas volume fraction and a halogen spot of 1000 W for higher volume fractions. The exposure time varies from 1/20000 s to 1/500 s depending on the lighting system.

In order to correctly account for truncated bubbles, it is necessary to perform a careful calibration to measure the optical aberration (image deformation near edges induced by the objective lens). The aberration on the optical installation used in Colombet et al. (2011) has been controlled, measured and shown to be negligible thanks to the use of an optical test calibrated pattern. For more details, the reader can refer to Colombet (2012). Otherwise, the aberration at image edges have to be corrected. If the aberration is too strong at image edges, it is then possible to crop the image to the area where image deformation at edge can be neglected and to use all the advantages of the algorithm by detecting truncated bubbles on the cropped image. But such a correction was not necessary here.

4.2. Results for air bubbles rising in a liquid column

The size, the shape, the local velocities and the trajectories of real bubbles have been studied in this section using the image processing technique previously described.

4.2.1. Bubble trajectories
The new image treatment is compared to the original one in Fig. 13. The analysis is made on the same set of images. Clearly, this figure shows that detecting truncated and overlapping bubbles, it is possible to follow the trajectories of many more bubbles and for a longer time. Indeed, the present image processing is able to increase the amount of detected bubbles by 43%.

The trajectory of a single rising bubble in a low-viscosity liquid does not generally follow a straight line and its path depends on the Reynolds number, on the presence of surface active agents and on the liquid flow. Mougin et al. (2001) show that in the regime were bubbles exhibit an ellipsoidal shape, the bubbles may rise following a two dimensional zigzag, a spiral around a vertical axis

or a rocking motion, depending on the characteristic numbers of the system (bubble diameter, properties of the fluid...). Within a swarm, bubbles may exhibit a different behavior and the trajectory of each bubble is influenced by the trajectories of neighboring bubbles. In Fig. 13, most of the bubbles follow a straight line but some seem to be trapped in neighboring bubbles wake and may follow different trajectories like in the center of Fig. 13a. Let us notice that the size of the image is not big enough to conclude that the trajectory of these bubbles is significantly different from the trajectory of an isolated bubble.

As reported by Morente et al. (2018), the bubble velocity variance is of great interest for the validation of numerical simulations of dense bubbly flow. However, it is particularly difficult to obtain the measurement convergence of this quantity when applying particle tracking methods to bubbly flows. Considering the present experimental set up, Colombet et al. (2015) have measured variances of vertical (z) and horizontal (x) bubble velocities with the original algorithm. Those results are reported on Fig. 14. The results obtained with the present new algorithm are also plotted on Fig. 14. It is found that the variance on vertical velocity V(Vz) matches with the one measured by Colombet et al. (2015) and stay quite constant while α increases, in agreement with the behavior of the variance measured with optical probe by Riboux et al. (2010). Concerning the variance of horizontal velocity V(Vx), the same order of magnitude is found but some discrepancies can be observed. The new algorithm that takes into account more bubbles along a longer path seems to suggest a weak increase of V(Vx) with α.

4.2.2. Bubble equivalent diameter
Along a sequence of images, it is possible to record the dimensions of each individual bubble in order to provide the bubble equivalent size distribution and to calculate averaged parameters such as the averaged bubble equivalent diameter $\widetilde{D}_{eq} = \langle D_{eq\,j} \rangle$. Following Colombet et al. (2015), the equivalent diameter of a bubble 'j', corresponds to the diameter of the sphere having the same volume as the measured prolate ellipsoid so that $D_{eq\,j} = (8a_j b_j^2)^{1/3}$, where a_j and b_j are respectively the semi-minor axis and the semi-major axis of the bubble j. Note that each individual bubble is counted only once even if present on successive images and the values of a_j and b_j are averaged along the detected bubble trajectory. The dimensionless average equivalent diameter D_{avg}^*, is de-
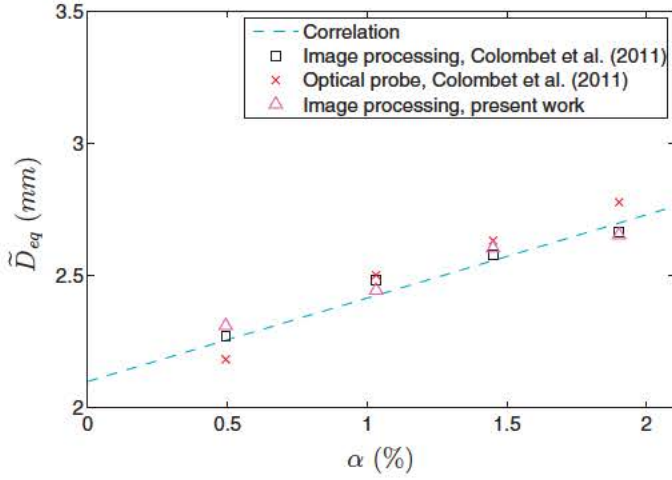
Fig. 16. Average equivalent diameter $\widetilde{D}_{eq}$ in mm as a function of the void fraction α. (- . -) correlation of Colombet et al., 2011 $(\widetilde{D}_{eq} - D_{eq0})/D_{eq0} = 15\alpha$ with $D_{eq0} = 2.1$ mm , ($\square$) Image processing by Colombet et al., 2011, ($\times$) dual-tip Optical probe data by Colombet et al., 2011 and ($\triangle$) present work.
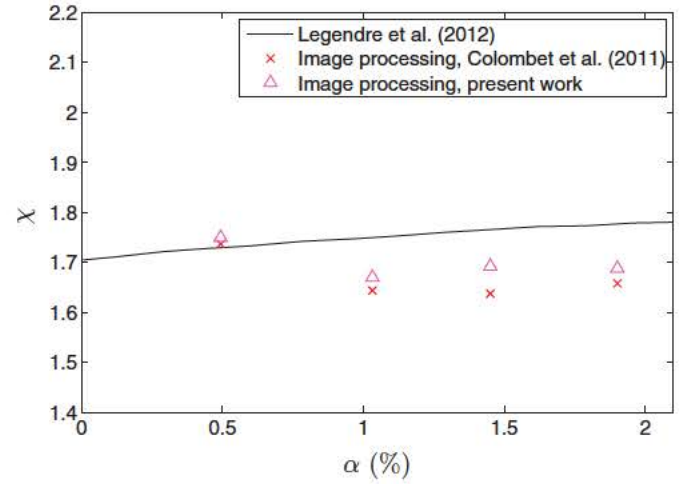

Fig. 17. Histogram envelope of the equivalent diameter D_{eq} for different void fractions α.

fined as:

$$D^*_{\text{avg}}(N_i) = \frac{1}{N_b \, \widetilde{D}_{eq}} \sum_{j=1}^{N_b} D_{eq\,j} = \frac{1}{N_b \, \widetilde{D}_{eq}} \sum_{j=1}^{N_b} (8 \, a_j b_j^2)^{1/3} \qquad (5)$$

where N_b is the number of detected bubbles for N_i images, and $\widetilde{D}_{eq}$ is the final average equivalent diameter. D^*_{avg} is reported in Fig. 15 as a function of the number of images N_i. For 6144 images, the present algorithm is able to detect 784 bubbles whereas the original algorithm only detects 486 bubbles. To achieve the measurement convergence at a 1% accuracy, the algorithm of Colombet et al. (2011) requires to process $\sim$3800 images whereas the present algorithm only requires $\sim$2250 images. This capability is put in evidence in Fig. 16 where $\widetilde{D}_{eq}$ (plotted versus the void fraction α) obtained with one set of 6144 images is compared with the results from Colombet et al. (2011) with four sets of images i.e. 24,576 images. The difference is only 2%. As expected, $\widetilde{D}_{eq}$ increases when α increases due to inertial effects increase at bubble detachment. Note also that it confirms the validity of the correlation proposed by Colombet et al. (2011) to predict bubble size. The histogram envelopes of the equivalent diameter for different void fractions are reported in Fig. 17. They show that the bubble diam-

Fig. 18. Average aspect ratio χ as a function of α. (—) Legendre et al. (2012), ($\times$) Colombet et al. (2011) and ($\triangle$) present work.
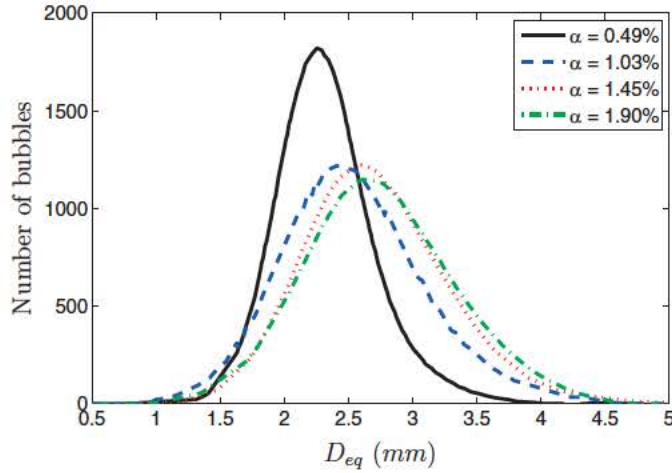
eters in the swarms are distributed around a major peak with a standard deviation of 10 % of the average value.

4.2.3. Bubble aspect ratio

We finally consider the bubble aspect ratio ($\chi = b/a$). The average aspect ratio is plotted as a function of α in Fig. 18. The figure shows that the results obtained with the present image treatment are also in agreement with previous results of Colombet et al. (2011) that slightly differ from the correlation of Legendre et al. (2012) proposed for single bubble. It also highlights that the average aspect ratio does not depend on the void fraction for the operating conditions investigated here and the void fraction considered ($\alpha \leq 2\%$).

5. Conclusion

In this work, an improved image processing method was developed to determine the size, the shape, the trajectory and the velocity of bubbles in bubbly flows. The method is based on an algorithm created by Riboux et al. (2010) and adapted by Boulesteix (2010) and Bouche et al. (2012) which allows indentifying bubbles in a gray-scale image. The values of the gray level gradients at each pixel are calculated and it is assumed that high gradient values correspond to the contour of *in focus* bubbles. Using a test on the convexity of the bubble contour added by Colombet et al. (2011), the original algorithm was able to detect in a bubble swarm single bubbles distant from the image edges, but it was unable to capture overlapping bubbles and truncated bubbles located in the neighborhood of the image edges. As a consequence, when the void fraction increases (and the number of bubbles per image increases), this algorithm requires a very large amount of images to ensure statistical convergence of data.

Therefore, an algorithm to account for the truncated and overlapping bubbles has been presented. By considering that the bubble shape can be approximated by ellipsoids, the truncated bubbles are approximated by ellipses whose properties are determined by performing an elliptical regression of the bubble contour points. The overlapping bubbles are separated using the *Watershed* algorithm proposed by Meyer (1994). To prevent the over-segmentation that causes measurement errors, a technique to identify the inflection points on object contours was implemented. Using the latter, overlapping bubbles can be separated and it is possible to verify whether or not the segmentation is correctly done. By this way, it is now possible to follow bubbles on longer trajectories, to better calculate their velocities.

The image processing techniques have been evaluated with synthetic images with 1 to 5 ellipses per image. By taking into account truncated and overlapping objects, 40% more ellipses can be identified and measured, leading to accurate results with a less number of images. A good agreement with the main results of Colombet et al. (2011, 2015) is also observed for an air/water bubble column but with the use of half of images.

Acknowledgements

References

Akita, K., Yoshida, F., 1974. Bubble size, interfacial area, and liquid-phase mass transfer coefficient in bubble columns. Ind. Eng. Chem., Process Des. Develop. 13 (1), 84–91.

Beucher, S., Lantejoul, C., 1979. Use of watersheds in contour detection. In: Proc. Int'l. Workshop on Image Proc., CCETT, Rennes, France.

Bouche, E., Roig, V., Risso, F., Billet, A.M., 2012. Homogeneous swarm of high-reynolds-number bubbles rising within a thin gap. Part 1: bubble dynamics. J. Fluid Mech. 704, 211–231.

Boulesteix, S., 2010. Cisaillement d'une interface gaz-liquide en conduite et entraînement de gouttelettes. Université Paul Sabatier, IMFT PhD thesis.

Burckhart, R., Deckwer, W., 1975. Bubble size distribution and interfacial area of electrolyte solutions in bubble columns. Chem. Eng. Sci. (Shorter Commun.) 30, 351–354.

Calderbank, P., 1958. Physical rate processes in industrial fermentation, part 1: the interfacial area in gas-liquid contacting with mechanical agitation. Trans. Inst. Chem. Eng. 36, 443–463.

Clift, R., Grace, J., Weber, M., 1978. Bubbles, Drops and Particulates. San Diego, Academic Press.

Colombet, D., 2012. Modélisation de réacteurs gaz-liquide de type colonne à bulle en conditions industrielles. Institut National des Sciences Appliquées de Toulouse (INSA Toulouse) PhD thesis.

Colombet, D., Legendre, D., Cockx, A., Guiraud, P., Risso, F., Daniel, C., Galinat, S., 2011. Experimental study of mass transfer in a dense bubble swarm. Chem. Eng. Sci. 66, 3432–3440.

Colombet, D., Legendre, D., Risso, F., Cockx, A., Guiraud, P., 2015. Dynamics and mass transfer of rising bubbles in a homogenous swarm at large gas volume fraction. J. Fluid Mech. 763, 254–285.

Davies, E., 1987. A high speed algorithm for circular object location. Pattern Recognit. Lett. 6 (5), 323–333.

Duda, R., Hart, P., 1972. Use of the hough transformation to detect lines and curves in pictures. Commun. ACM 15, 204–208.

Duineveld, P., 1995. The rise velocity and shape of bubbles in pure water at high reynolds number. J. Fluid Mech. 292, 325–332.

Ellingsen, K., Risso, F., 2001. On the rise of an ellipsoidal bubble in water: oscillatory paths and liquid-induced velocity. J. Fluid Mech. 440, 235–268.

Faria, N., Pons, M., Feyo de Azevedo, S., Rocha, F., Vivier, H., 2003. Quantification of the morphology of sucrose crystals by image analysis. Powder Technol. 133, 54–67.

Fereira, A., Pereira, G., Teixeira, J., Rocha, F., 2012. Statistical tool combined with image analysis to characterize hydrodynamics and mass transfer in a bubble swarm. Chem. Eng. J. 180, 216–228.

Fu, Y., Liu, Y., 2016. Development of a robust image processing technique for bubbly flow measurement in a narrow rectangular channel. Int. J. Multiphase Flow 84, 217–228.

Halíř, R., Flusser, J., 1998. Numerically stable direct least squares fitting of ellipses. Winter School Comput. Graph. 6.

Honkanen, M., Saarenrinne, P., Stoor, T., Niinimäki, J., 2005. Recognition of highly overlapping ellipse-like bubble images. Meas. Sci. Technol. 16, 1760–1770.

Kumar, A., Degaleesan, T., Laddha, G., Hoelscher, H., 1976. Bubble swarm characteristics in bubble columns. Can. J. Chem. Eng. 54, 503–508.

Lantejoul, C., Beucher, S., 1981. On the use of the geodesic metric in image analysis. J. Microscopy.

Lau, Y., Deen, N., Kuipers, J., 2013. Development of an image measurement technique for size distribution in dense bubbly flows. Chem. Eng. Sci. 94, 20–29.

Legendre, D., Zenit, R., Velez-Cordero, J., 2012. On the deformation of gas bubbles in liquids. Phys. Fluids 24, 043303.

Marmottant, P., 2001. Atomisation d'un jet liquide par un courant gazeux. Institut National Polytechnique de Grenoble.

Meyer, F., 1994. Topographic distance and watershed lines. Signal Processing 38, 113–125.

Morente, A., Laviéville, J., Legendre, D., 2018. A penalization method for the simulation of bubbly flows. J. Comput. Phys. 374, 563–590.

Mougin, G., Magnaudet, J., 2001. Path instability of a rising bubble. Phys. Rev. Lett. 88 (1). Bubble P. i. o. a. r.

Otsu, N., 1979. A threshold selection method from gray-level histograms. IEEE Trans. Syst. SMC-9, 62–66.

Pla, F., 1996. Recognition of partial circular shapes from segmented contours. Comput. Vision Image Understanding 63 (2), 334–343.

Prewitt, J., 1970. In: Lipkin, B., Rosenfeld, A. (Eds.), Object enhancement and extraction, picture processing and psychopictorics. Academic Press, New York, pp. 75–149.

Riboux, G., 2007. Hydrodynamique d'un essaim de bulles en ascension. INP Toulouse Ph. D Thesis.

Riboux, G., Risso, F., Legendre, D., 2010. Experimental characterization of the agitation generated by bubbles rising at high reynolds number. J. Fluid Mech. 643, 509–539.

Roberts, L., 1965. In: Tippet, J.T., et al. (Eds.), Machine perception of three-dimensional solids, optical and electro-optical information processing. Cambridge, M. A. : MIT press, pp. 159–197.

Shen, L., Song, X., Iguchi, M., Yamamoto, F., 2000. A method for recognizing particles in overlapped particle images. Pattern Recognit. Lett. 21 (1), 21–30.

Sobel, I., 1970. Camera models and machine perception. Stanford Doctoral Dissertation.

Yianatos, J., Finch, J., Dobby, G., Xu, M., 1987. Bubble size estimation in a bubble swarm.. J. Colloid Interface Sci. 126 (1), 37–44.

Zhang, W., Jiang, X., Liu, Y., 2012. A method for recognizing overlapping elliptical bubbles in bubble image. Pattern Recognit. Lett. 33 (12), 1543–1548.